analytical chemistry

pubs.acs.org/ac Article

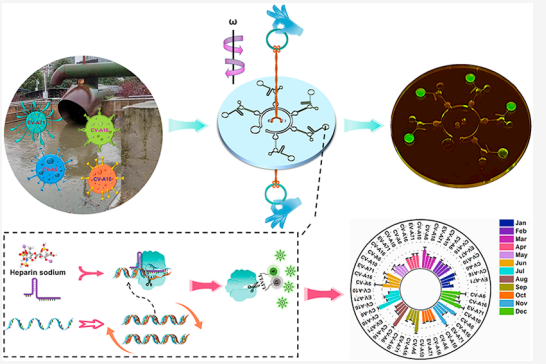
String-Powered Microfluidic Chip Integrating Heparin-Mediated One-Pot RT-RPA/CRISPR-Cas12a for Multiplex Detection of HFMD Viruses

Zhen Chen, Kang Mao,* Hanqing Meng, Chen Gao, Haoran Lv, Xiqing Li, Qiuda Zheng, Zhugen Yang, Ibrahim Ahmed Hamza, Chenglong Tu,* and Hua Zhang

Cite This: https://doi.org/10.1021/acs.analchem.6c00663 Read Online

ACCESS | Metrics & More | Article Recommendations | Supporting Information

ABSTRACT: Hand, foot, and mouth disease (HFMD) is a common childhood infection caused by enteroviruses, which exhibit distinct regional and seasonal epidemiological patterns. Wastewater-based epidemiology is a crucial tool for monitoring population infection dynamics and viral subtype distribution. However, the lack of effective on-site viral detection methods limits timely early warning and effective surveillance of infectious disease outbreaks. This study developed a one-pot RT-RPA/CRISPR-Cas12a assay-based, string-powered flywheel microfluidic chip for the multiplex detection of HFMD viruses in wastewater. First, by leveraging the regulatory effect of heparin sodium on CRISPR/Cas12a activity, a one-pot RT-RPA/CRISPR-Cas12a system was constructed to detect four major subtypes of HFMD virus (EV-A71, CV-A16, CV-A6, and CV-A10). Subsequently, this method was integrated into a pull-wire, flywheel-type, dual-axis centrifugal microfluidic chip, named the Heparin-Inhibited CRISPR-Associated System Chip (HICAS-Chip), enabling integrated enrichment, purification, elution, and multiplexed detection. The HICAS-Chip allowed visual detection of nucleic acids at 10 aM sensitivity within 1 h, corresponding to the sensitivity of the one-pot RT-RPA/CRISPR-Cas12a assay. During a year-long wastewater monitoring program in Guiyang City, China, the HICAS-Chip identified EV-A71 and CV-A10 as the predominant circulating subtypes, with incidence peaks observed in June, November, and December. The wastewater detection results obtained using HICAS-Chip showed high concordance (95.83%) with RT-qPCR assays. This platform provides an efficient portable device for the early detection and continuous monitoring of HFMD epidemic trends by wastewater-based epidemiology.



Downloaded via SHANGHAI NORMAL UNIV on May 5, 2026 at 14:01:29 (UTC).
See https://pubs.acs.org/sharingguidelines for options on how to legitimately share published articles.

INTRODUCTION

Hand, foot, and mouth disease (HFMD) is a widespread infectious disease with a high incidence among children under the age of five, caused by enteroviruses, and can result in neurological complications or even death.[1−4] Moreover, its epidemiological trends show a gradual increase in both incidence and mortality rates, thereby intensifying the burden of prevention and control in densely populated areas and heightening the risk of infection in regions with low economic levels and inadequate healthcare resources.[5,6] The primary subtypes responsible for HFMD are Enterovirus A71 (EV-A71), Coxsackievirus A16 (CV-A16), Coxsackievirus A6 (CV-A6), and Coxsackievirus A10 (CV-A10).[7] Therefore, early surveillance of these four viral subtypes is crucial for anticipating epidemic waves and timely public health responses, informing effective prevention measures.

Wastewater-based epidemiology is an effective approach for the early warning of infectious disease transmission and outbreaks.[8] By analyzing infectious disease biomarkers in wastewater collected from defined catchment areas, disease transmission within communities can be monitored in near real time.[9] For instance, during the COVID-19 pandemic, numerous laboratories worldwide monitored SARS-CoV-2 RNA in wastewater to explore its potential as a population-level management and early warning tool.[10] Our team successfully achieved semiquantitative detection of SARS-CoV-2 in wastewater using an in-house-developed paper-based analytical device, further demonstrating the practical feasibility of such surveillance approaches.[11,12] Supporting this approach, Shrestha et al.[13,14] revealed seasonal patterns and dominant viral subtypes in HFMD studies across South Asia and Japan, demonstrating that detecting enteroviruses in wastewater can serve as a cost-effective approach for predicting community infection trends.

Received: January 27, 2026
Revised: April 2, 2026
Accepted: April 30, 2026

ACS Publications © XXXX American Chemical Society

The ultimate goal of wastewater-based epidemiology is to achieve on-site monitoring and provide real-time data, which is essential for early warning of infectious disease outbreaks. Therefore, analytical tools for wastewater-based epidemiology should be simple, rapid, cost-effective, sensitive, selective, and capable of multiplex detection. However, the gold standard for pathogen detection, polymerase chain reaction (PCR), requires precise temperature control and laboratory conditions during testing, which limits its applicability to on-site surveillance in resource-limited settings.[15] Therefore, the development of sensitive detection technologies and portable devices is crucial for advancing the widespread use of wastewater surveillance in public health.[16]

Recently, the clustered regularly interspaced short palindromic repeats (CRISPR)-associated (Cas) system has demonstrated tremendous potential in the field of rapid diagnostics, due to its high targeting specificity and programmable recognition capabilities.[17] CRISPR/Cas identifies target sequences via specific crRNAs, which activate the trans-cleavage activity of Cas nucleases, enabling signal output and visual detection. However, the standalone CRISPR/Cas system still faces the challenge of relatively low sensitivity, making it difficult to effectively identify low-abundance targets in complex samples, such as wastewater. To overcome this limitation, CRISPR/Cas systems are commonly integrated with isothermal nucleic acid amplification. Among these, recombinase polymerase amplification (RPA) exhibits temperature compatibility with CRISPR/Cas reactions, offering great potential for point-of-care testing.

Despite these advantages, incompatibilities between RPA and CRISPR/Cas arise from differences in buffer composition and reaction kinetics, often leading to mutual interference, thereby hindering their seamless integration within a single reaction system. Consequently, most CRISPR-based diagnostic platforms adopt a stepwise workflow, in which RPA first amplifies nucleic acids, followed by CRISPR/Cas-based recognition and detection of the amplified product. Representative platforms such as SHERLOCK[18] and DETECTR[19] embody this combined approach. However, the two-step workflow remains relatively laborious and time-consuming, and frequent lid-opening operations increase the risk of aerosol contamination.[20,21]

To address these limitations, the integration of RPA and CRISPR/Cas into a one-pot system has become essential for point-of-care testing. Current integration strategies mainly involve physical separation of reactions, enhancing RPA amplification efficiency or modifying crRNA structures. Approaches such as RNase H supplementation,[22] primer and buffer optimization,[23] and crRNA engineering[24−27] can effectively reduce premature Cas12a activity but increase experimental complexity and costs. Consequently, Cheng et al.[28] proposed the use of heparin sodium to competitively inhibit Cas12a-crRNA interactions. This approach balances the amplification and recognition/cleavage reactions in a one-pot assay.

In practical wastewater analysis, complex pretreatment and detection processes are further challenged due to the complex wastewater matrices and the dilution of viral particles. Consequently, wastewater testing usually involves laborious pretreatment steps, including virus concentration and lysis, and nucleic acid enrichment, purification and elution, which hinder the direct application of molecular detection techniques in point-of-care testing.[29] To overcome these limitations, strategies that integrate multiple steps, including sample pretreatment, detection, and signal output, into multifunctional modular reactions are required.

Microfluidics, often referred to as lab-on-a-chip systems, enables the precise manipulation of fluids at the micro- and nanoscale.[30,31] This facilitates the integration of multiple steps, from sample pretreatment to nucleic acid amplification and detection within a single platform. Owing to their high integration, miniaturization, portability and reduced reagent consumption, microfluidic devices are well suited to advancing CRISPR-based isothermal nucleic acid amplification techniques toward point-of-care testing.[32−34] However, many reported CRISPR-based microfluidics lack integrated pretreatment modules, limiting their applicability for wastewater analysis.[35,36]

Lab-on-a-disc is a branch of microfluidic devices that offers unique advantages due to its compact design and efficient centrifugal fluid control.[37,38] Classic lab-on-a-disc systems rely on externally powered centrifuges, which restrict portability.[39−41] In contrast, string-powered flywheel systems provide a low-cost, instrument-free actuation strategy capable of bidirectional rotation. Notably, Bhamla et al. demonstrated that such mechanisms can generate sufficient centrifugal forces for high-efficiency separation, highlighting their potential for portable microfluidic devices.[42]

Herein, we developed an integrated microfluidic chip based on heparin sodium-mediated one-pot RT-RPA/CRISPR-Cas12a system for the multiplex detection of four major HFMD viruses in wastewater. The assay is fully integrated with a string-powered, dual-axis centrifugal microfluidic device, the Heparin-Inhibited CRISPR-Associated System Chip (HICAS-Chip), which enables on-chip nucleic acid capture, washing, elution and detection without external instrumentation while effectively preventing false positives from aerosol contamination. The platform was validated through a year-long wastewater-based surveillance trial at a wastewater treatment plant in Guiyang City, China. Its results were compared to those of standard RT-qPCR, highlighting its potential as a simple, portable tool for HFMD surveillance by wastewater-based epidemiology.

EXPERIMENTAL SECTION

Materials

The LbCas12a protein was prepared in-house, while the RPA kit was purchased from Qitian-Gene Biotechnology Co., Ltd. Nuclease-free water, primers, FAM-labeled reporter probe, heparin sodium, T7 RNA polymerase, M-MuLV reverse transcriptase and RNA-purification magnetic beads were obtained from Sangon Biotech (Shanghai) Co., Ltd. The crRNA was synthesized by Guangzhou Boliase Biotechnology Co., Ltd., the PCR kit was sourced from ToloBio Biotech Co., Ltd., and the plasmid and RNA purification kits were purchased from Tiangen Biotech (Beijing) Co., Ltd. Thermal cycling for PCR was performed using ABI 7500 real-time quantitative PCR system (Thermo Fisher Scientific). The water-sample RNA extraction kit was supplied by Guangzhou Jiebeisi Biotechnology Co., Ltd.

Preparation of Plasmids and In Vitro Transcription

Conserved sequences of EV-A71 (GenBank FN665373.1), CV-A16 (GenBank OQ626555.1), CV-A6 (GenBank MG385831.1) and CV-A10 (GenBank MK965242.1) were retrieved from the National Center for Biotechnology Information. Sequence specificity was verified using the Basic Local Alignment Search Tool. The verified sequences were chemically synthesized and ligated into the pUC57 vector to generate recombinant plasmids carrying ampicillin

https://doi.org/10.1021/acs.analchem.6c00663
Anal. Chem. XXXX, XXX, XXX−XXX

resistance. Full plasmid construction was carried out by Sangon Biotech Co., Ltd. DNA concentrations were measured using an Invitrogen Qubit 4 fluorometer (Thermo Fisher Scientific).

Design of Primers, crRNA, and ssDNA Reporter

Based on the conserved sequences of the four enterovirus subtypes (EV-A71, CV-A16, CV-A6, and CV-A10), four pairs of subtype-specific RPA primers for each virus were designed in accordance with the RPA primer-design guidelines (Supporting Table 1). Primer sets producing uniformly bright amplification bands were selected. Subsequently, crRNAs were designed for the corresponding amplicon regions; each crRNA comprises a spacer sequence that matches the target and a highly conserved repeat region. During isothermal fluorescence detection, a FAM-BHQ-labeled single-stranded DNA (ssDNA) serves as the reporter. The sequences of the crRNAs and the FAM-labeled reporter probes are listed in Supporting Table 2.

Construction of RT-RPA and CRISPR/Cas12a-Based One-Pot Assay

For the construction of the RT-RPA reaction system, 25 μL of Buffer V was used to hydrate the lyophilized reaction pellet. Subsequently, forward and reverse primers were added to a final concentration of 400 nM, together with 16 μL of sterile, nuclease-free water and the template to be tested, yielding a reaction volume of 45 μL. The reaction was then initiated by adding 5 μL of Magnesium Acetate I and incubated at 37 °C for 30 min. Upon completion, an equal volume of a phenol/chloroform mixture (1:1) was added to the tube, mixed thoroughly by vortexing, and centrifuged for phase separation. The aqueous phase containing the amplified product was collected for subsequent analysis.

In the CRISPR/Cas12a assay, Cas12a and crRNA were added to a final concentration of 100 nM, together with a 500 nM FAM-labeled reporter probe, 2 μL of 10× NEBuffer 2.1, and nuclease-free sterile water to a total volume of 20 μL. This system enables specific target recognition and collateral cleavage for signal generation.

For the heparin sodium-based one-pot assay, 1 nM targeted RNA was selected as the target analyte. Using a controlled-variable approach, we optimized the heparin sodium concentration, crRNA-to-Cas12a molar ratio, reporter probe concentration, and M-MuLV reverse transcriptase concentration. Heparin sodium was tested at concentrations of 10, 20, 30, 40, 50, and 60 $\mu g \cdot mL^{-1}$. The final concentration of Cas12a was fixed at 100 nM, while the crRNA concentration was varied to achieve crRNA: Cas12a ratios of 1:2 (50 nM), 1:1 (100 nM), 2:1 (200 nM), 3:1 (300 nM), and 4:1 (400 nM). The FAM-labeled reporter probe was set at 200, 300, 400, 500, 600, 700, and 800 nM. M-MuLV reverse transcriptase was added at final activities of 40, 50, 60, 70, and 80 U. The assembled RT-RPA/CRISPR system was incubated at 39 °C for 1 h, after which fluorescence was measured with the ABI 7500 instrument.

Design, Fabrication and Performance Evaluation of the HICAS-Chip

The microfluidic chip designed in this study was modeled using computer-aided design software and exported in.dwg format. The chip substrate was fabricated from poly(methyl methacrylate) (PMMA) via CO_2 laser cutting, with production outsourced to YoungChip Technology Co., Ltd. The chip has a diameter of 7 cm and a thickness of 4 mm. Two through-holes, each 2 mm in diameter, are positioned at the center of the string-driven centrifugal mechanism. Microchannel widths range from 0.15 mm to 1 mm, and the chamber diameters range from 2 mm to 6 mm. The PMMA substrate and a pressure-sensitive adhesive layer were laminated by roller-press bonding to form a sealed microfluidic structure.

After the magnetic beads and the glass-fiber membrane are preloaded into the HICAS-Chip, a single-sided pressure-sensitive adhesive sealing film is applied to effectively seal the point where the chip contacts the external atmosphere. Within this sealed system, the pressure variation follows the ideal-gas law

$$PV = nRT \tag{1}$$

where P denotes the pressure, V is the gas volume, n represents the amount of gas in moles, R is the ideal-gas constant, and T is the temperature.

Fluid actuation relies on the combined effects of pressure variation, capillary regulation, and centrifugal force. The flow of liquid in the microchannels obeys the Hagen−Poiseuille equation

$$Q = \frac{\pi r^4}{8\mu L}\Delta P \tag{2}$$

where Q denotes the volumetric flow rate, r is the channel radius, μ represents the liquid viscosity, L is the channel length, and ΔP is the pressure difference between atmospheric pressure and the internal pressure of the chip. The capillary threshold pressure is described by the Young−Laplace equation

$$\Delta P_{cap} = \frac{2\gamma \cos\theta}{r_p} \tag{3}$$

where γ denotes the liquid surface tension, θ is the contact angle, and r_p is the pore radius. When θ exceeds 90°, the hydrophobic surface forms an effective capillary valve, and liquid can pass only when the applied pressure difference is greater than $|\Delta P_{cap}|$. The chip achieves rotation without an external motor by winding and unwinding a hemp rope. The centrifugal pressure difference experienced by the liquid at a radius r is

$$\Delta P_{centrifugal} = \frac{1}{2}\rho\omega^2 r^2 \tag{4}$$

$$\omega = \sqrt{\frac{2Fs}{I}} \tag{5}$$

$$I = \frac{mr^2}{2} \tag{6}$$

$$N(\mathrm{rpm}) = \frac{60\omega}{2\pi} \tag{7}$$

where ρ denotes the liquid density, ω denotes the angular velocity, F denotes the pulling-line tension force, s denotes the pulling-line length, I denotes the moment of inertia, m denotes the chip mass, and N denotes the rotational speed.

In addition, pressure regulation plays an important role in controlling the accessibility of the elution chamber. When the elution chamber remains sealed, the internal gas volume remains constant, resulting in a relatively higher internal pressure compared with the punctured washing chamber depending on eq 1. Together with the hydrophobic capillary barrier described in eq 3, this pressure difference prevents liquid from entering the elution chamber during the washing process. Only after the pressure-sensitive adhesive (PSA) layer above the elution chamber is punctured can the internal pressure be rebalanced, allowing the elution buffer and nucleic acids to enter the chamber under centrifugal actuation.

To assess the analytical performance of HICAS-Chip for HFMD virus, the four viral subtype plasmids (EV-A71, CV-A16, CV-A6, and CV-A10) were transcribed in vitro. RNA concentrations were measured using a Qubit 4 fluorometer, and then serially diluted from 10 fM to 0.1 aM (10 fM, 1 fM, 100 aM, 10 aM, 1 aM and 0.1 aM). To determine specificity and interference resistance, each target was tested in the presence of the other virus subtypes using the one-pot assay. Fluorescence signals were measured using an ABI 7500 instrument.

To evaluate manual operation variability, five operators independently performed the HICAS-Chip detection procedure using the same sample (EV-A71, 100 aM). Each operator conducted four replicate experiments. The operators included three males (operators A-C) and two females (operators D-E), aged between 20 and 40 years. Fluorescence images were analyzed using ImageJ to obtain mean *RGB* intensity values. The detection threshold was defined as the mean fluorescence intensity of the negative control plus three standard deviations, and the coefficient of variation was calculated.

https://doi.org/10.1021/acs.analchem.6c00663
Anal. Chem. XXXX, XXX, XXX−XXX

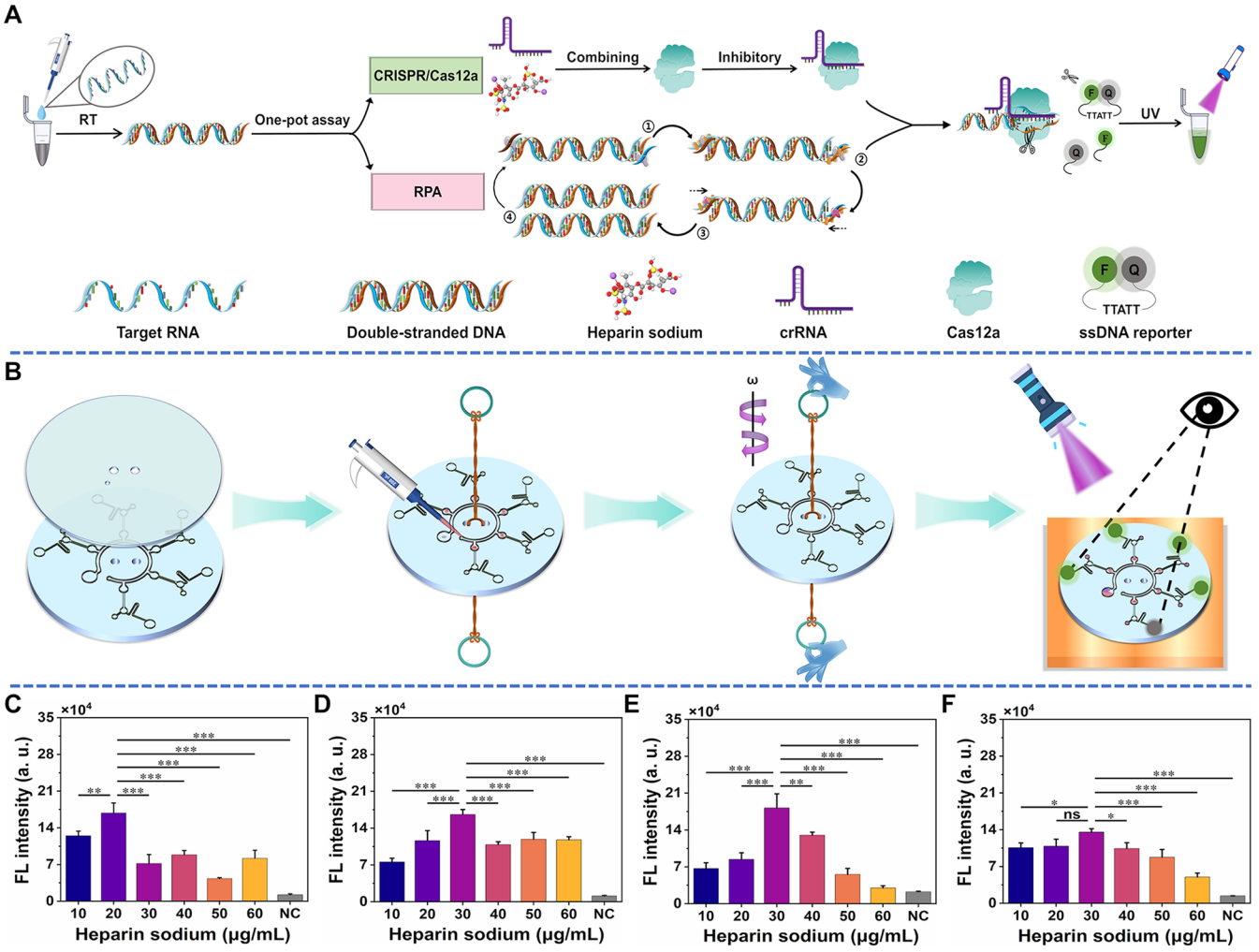


Figure 1. Principle of the heparin sodium-mediated one-pot RT-RPA/CRISPR assay implemented on the HICAS-Chip. (A) Schematic illustration of the heparin-mediated one-pot RT-RPA/CRISPR-Cas12a assay. Viral RNA is reverse-transcribed and amplified via RPA, followed by Cas12a-mediated trans-cleavage of a FAM-labeled reporter to produce a detectable fluorescence under UV light. (B) Workflow of the HICAS-Chip. The integrated platform combines magnetic bead-based nucleic acid extraction with the one-pot RT-RPA/CRISPR-Cas12a assay. A rope-driven flywheel and pressure-sensitive membranes control fluid dynamics, while a microheating pad ensures optimal reaction temperatures for visual detection under UV light. (C–F) End-point fluorescence values obtained with heparin-sodium concentrations ranging from 10 μg mL^{-1} to 60 μg mL^{-1} for a constant 1 nM RNA template of (C) EV-A71, (D) CV-A16, (E) CV-A6, and (F) CV-A10. Data are presented as mean ± SD (n = 3). Statistical significance is indicated as ns, $p > 0.05$; *, $p < 0.05$; **, $p < 0.01$; ***, $p < 0.001$.

Wastewater Collection and Off-Chip Pretreatment

Wastewater influent samples were collected from the Jinyang Wastewater Treatment Plant (106.6439°E, 26.5948°N) in Guiyang City throughout 2024, including monthly sampling and daily sampling within 1 week during incidence peaks in June and December, yielding 24 samples. For viral concentration, samples were first prefiltered to remove large suspended solids using a 10 μm filter membrane. Viral particles were then concentrated from 250 mL of wastewater by filtration through a 0.22 μm cellulose acetate membrane. Before filtering, the wastewater was adjusted to pH 3.5 with 1 M HCl. Then 1 M $MgCl_2$ was added to promote Mg^{2+}-mediated electrostatic bridging between negatively charged viral particles and the cellulose acetate membrane. Finally, the cellulose acetate membrane containing virus particles was processed using a commercial water-sample RNA extraction kit, yielding a final RNA solution of 100 μL. This standardized procedure allows better evaluation of the HICAS-Chip performance in wastewater while reducing variability introduced during sample preprocessing, including virus concentration and lysis.

Analytical Performance and Wastewater Surveillance of HFMD Viruses

To test the recovery rate of the HICAS-Chip, spike experiments were performed by adding HFMD viral RNA at 0, 10 aM, 100 aM, and 1 fM to lysed wastewater samples, resulting in a final volume of 100 μL. The wastewater matrix used for the spike recovery experiments was obtained from influent samples collected in January, representing real environmental samples used as the background matrix. All subsequent procedures followed the standard HICAS-Chip workflow. The calculated recovery rates only reflect the analytical processes of the HICAS-Chip. The off-chip pretreatment steps, including viral concentration and lysis, were not tested because they were performed using a standardized commercial kit protocol, and our objective was to specifically evaluate the analytical performance of the HICAS-Chip rather than the overall recovery from raw wastewater. Fluorescence images were analyzed using ImageJ (weighted RGB formula: $0.299R + 0.587G + 0.114B$), and recovery rates were calculated as follows

$$\text{recovery}\ (\%) = \frac{C_{\text{spiked}} - C_{\text{background}}}{C_{\text{added}}} \times 100\% \quad (8)$$

https://doi.org/10.1021/acs.analchem.6c00663
Anal. Chem. XXXX, XXX, XXX−XXX

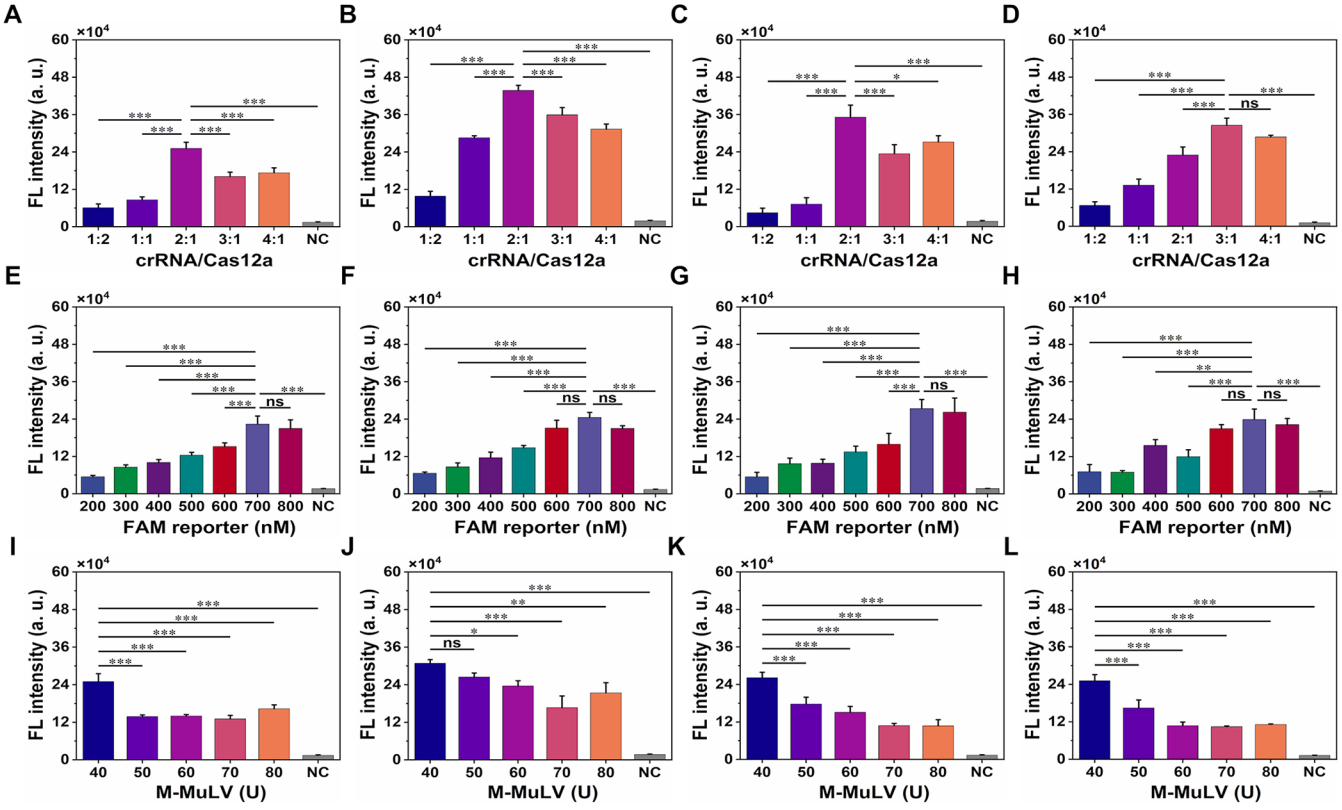


Figure 2. Optimization of key reagents in the one-pot assay. (A–D) The crRNA concentration was titrated while maintaining a fixed Cas12a concentration (100 nM) for EV-A71 (A), CV-A16 (B), CV-A6 (C), and CV-A10 (D). (E–H) Determination of the optimal concentration of the FAM-labeled reporter probe in the single-tube reaction for EV-A71 (E), CV-A16 (F), CV-A6 (G), and CV-A10 (H). (I–L) Evaluation of the impact of varying M-MuLV reverse-transcriptase concentrations on fluorescence intensity for EV-A71 (I), CV-A16 (J), CV-A6 (K), and CV-A10 (L). Data are expressed as mean ± SD (n = 3). Statistical significance: ns, $p > 0.05$; *, $p < 0.05$; **, $p < 0.01$; ***, $p < 0.001$.

To further evaluate the applicability of the HICAS-Chip for wastewater surveillance and to assess the prevalence of HFMD viral subtypes in the targeted area, a total of 24 wastewater samples were analyzed using the tube-based one-pot RT-RPA/CRISPR-Cas12a assay, the HICAS-Chip platform, and RT-qPCR.

For the tube-based one-pot assay, fluorescence signals were obtained from three parallel reactions per sample. A positivity threshold was defined as the mean fluorescence intensity of the negative control plus three standard deviations (mean ± 3SD). Samples with fluorescence signals above this threshold were classified as positive. For HICAS-Chip analysis, fluorescence images were captured by a smartphone and analyzed with ImageJ to obtain mean *RGB* values from each reaction chamber. The positivity threshold for on-chip detection was defined similarly as the mean ± 3SD of the negative control signals. The RT-qPCR was performed on the same wastewater samples to validate the developed method.

Statistics and Reproducibility

Data analysis and visualization were performed using Microsoft Excel 2021 and Origin Pro 2024. One-way analysis of variance was applied to test for overall differences among the independent groups. When significant differences were detected, Tukey's honestly significant difference was used, with statistical significance set at $\alpha < 0.05$. All experiments were performed with three independent replicates.

RESULTS AND DISCUSSION

Mechanism and Feasibility of HICAS-Chip

Figure 1 demonstrates the principle of the heparin sodium-mediated one-pot RT-RPA/CRISPR assay and HICAS-Chip. As shown in Figure 1A, the one-pot assay integrates reverse transcription of the RNA template, RPA, and CRISPR/Cas12a-driven cleavage in a single reaction. In the presence of the target, RPA is initiated by the coordinated action of recombinase, single strand binding proteins, and DNA polymerase, enabling rapid amplification. Concurrently, the crRNA binds to the PAM site of the target and guides Cas12a to cleave the DNA, thereby activating Cas12a's trans-cleavage activity. This activity indiscriminately cuts a FAM-labeled reporter probe, generating a fluorescent signal that can be detected. Because RPA is an exponential amplification process that typically reaches completion within 10–15 min, whereas Cas12a's target cleavage proceeds linearly, it is crucial to suppress premature Cas12a activity during the early phase of RPA. Adding heparin sodium creates a competitive interaction with crRNA for Cas12a binding, preventing loss of low-abundance targets before RPA amplification and thereby ensuring a reliable one-pot assay.

Following the one-pot assay, Figure 1B provides a schematic overview of the HICAS-Chip and corresponding operation. The illustration includes the assembly of the microfluidic chip, the loading of samples and reagents, and the manual actuation of the device by pulling a string to generate centrifugal force and control the rotation direction. After sample processing, the chip is placed on a simple heating plate to provide the temperature required for the one-pot reaction, and fluorescence signals are used for result interpretation. Detailed operating principles and workflow are described in the section Workflow and Performance of the Integrated HICAS-Chip Device.

https://doi.org/10.1021/acs.analchem.6c00663
Anal. Chem. XXXX, XXX, XXX−XXX

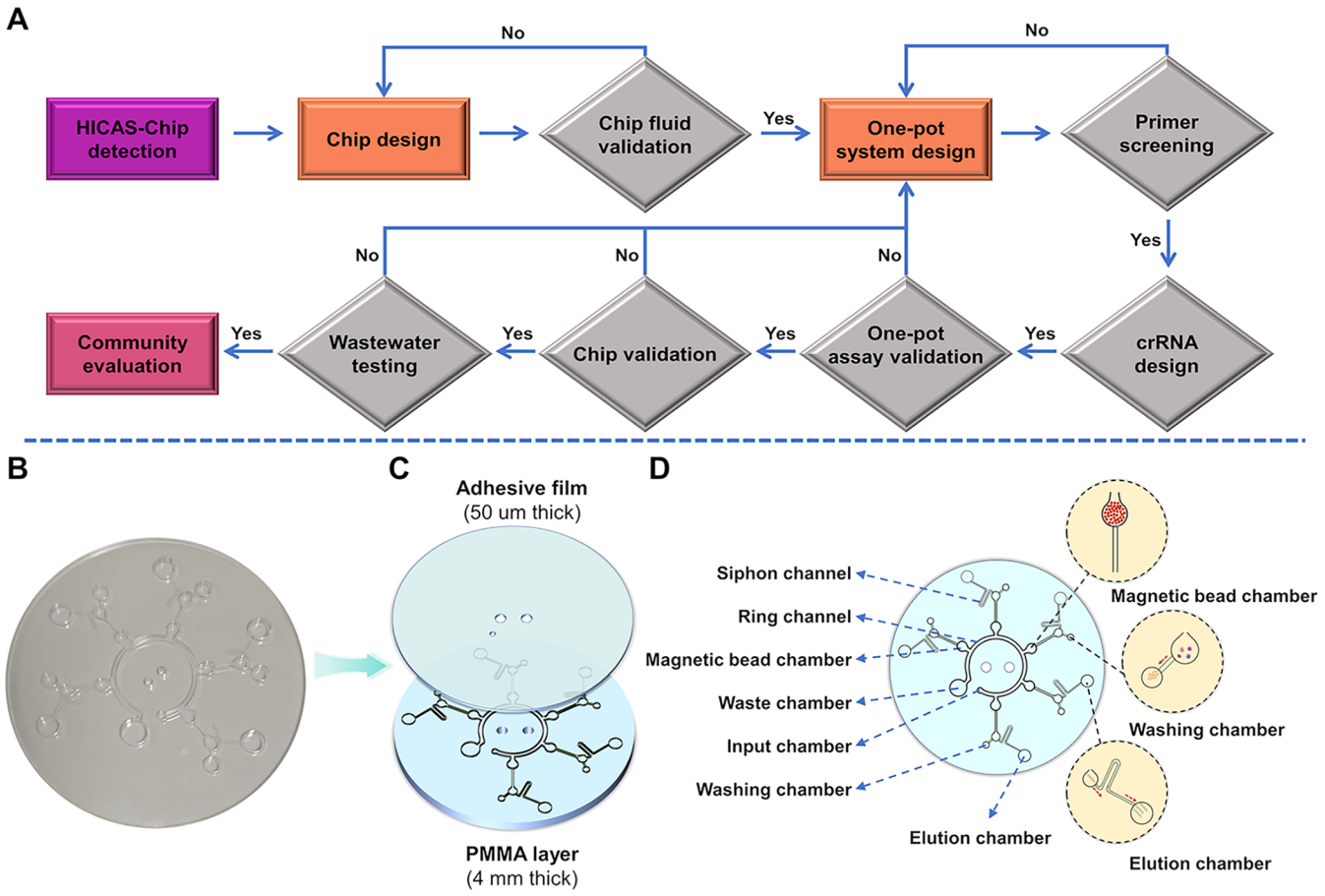


Figure 3. Design and fabrication of the HICAS-Chip. (A) An iterative design and optimization process of the HICAS-Chip to achieve stable fluid manipulation and integrated detection. (B) Photograph of the fabricated HICAS-Chip prototype. (C) Schematic illustration of the layered structure of the chip composed of a PMMA substrate and a PSA sealing film. (D) Layout of the PMMA microfluidic layer showing the annular main channel, magnetic bead chamber, washing and elution chambers, siphon valve, and waste reservoir.

To validate the regulatory role of heparin sodium, we first optimized its concentration in the one-pot assay. As illustrated in Figure 1C−F, fluorescence end point values for each target varied with heparin sodium concentration, displaying a single-peak profile: concentrations below or above the optimum yielded reduced signals. Statistical analysis identified the optimal heparin sodium concentrations as 20 μg mL^{-1} for EV-A71, 30 μg mL^{-1} for CV-A16 and CV-A6. Although the end-point fluorescence for CV-A10 showed no significant difference between 20 μg mL^{-1} and 30 μg mL^{-1}, the highest signal was observed at 30 μg mL^{-1}; which was therefore adopted.

Optimization of Heparin Sodium-Mediated One-Pot RT-RPA/CRISPR Assay

Analytical performance of the one-pot assay is strongly dependent on the concentrations of critical reagents: the crRNA, the FAM-labeled reporter probe, and the reverse-transcriptase M-MuLV. Herein, we systematically optimized these three parameters by fixing Cas12a concentration at 100 nM.

The optimization of crRNA concentration (Figure 2 A−D) revealed that 200 nM crRNA produced the strongest fluorescence peaks for the EV-A71, CV-A16, and CV-A6 assays. Dose−response analysis indicated that insufficient crRNA reduced its competitive binding to heparin sodium, thereby hindering the assembly of the CRISPR-Cas12a complex, whereas excessive crRNA can diminish the early inhibitory effect of heparin sodium on Cas12a activity. For the CV-A10 system, fluorescence signals at 300 nM and 400 nM were statistically indistinguishable. Considering cost efficiency and the slightly higher end-point fluorescence observed at 300 nM, we therefore selected 300 nM as the optimal concentration for this subtype.

The titration of the FAM-labeled reporter probe (Figure 2E−H) demonstrated a clear positive correlation between probe concentration and fluorescence intensity, with the 700 nM reporter probe yielding the highest signal for all four viral subtypes. Increasing the probe concentration beyond this point did not produce a statistically significant enhancement of the assay. Consequently, a probe concentration of 700 nM was adopted as the standard for all subsequent experiments. These concentrations were selected not only to maximize fluorescence signal for each HFMD viral subtype but also to minimize nonspecific cleavage and cross-reactivity, ensuring reliable and robust one-pot assay.

In the one-pot assay, the concentration of reverse-transcriptase is a pivotal parameter because viral RNA must be converted to cDNA before RPA amplification and Cas12a-mediated cleavage can occur. To assess its impact, we used M-MuLV reverse-transcriptase (60 U as the reference) and varied its amount by adding or subtracting nuclease-free water while keeping all other reagents constant. As shown in Figure 3 I−L, increasing the enzyme dose did not appreciably change the

https://doi.org/10.1021/acs.analchem.6c00663
Anal. Chem. XXXX, XXX, XXX−XXX

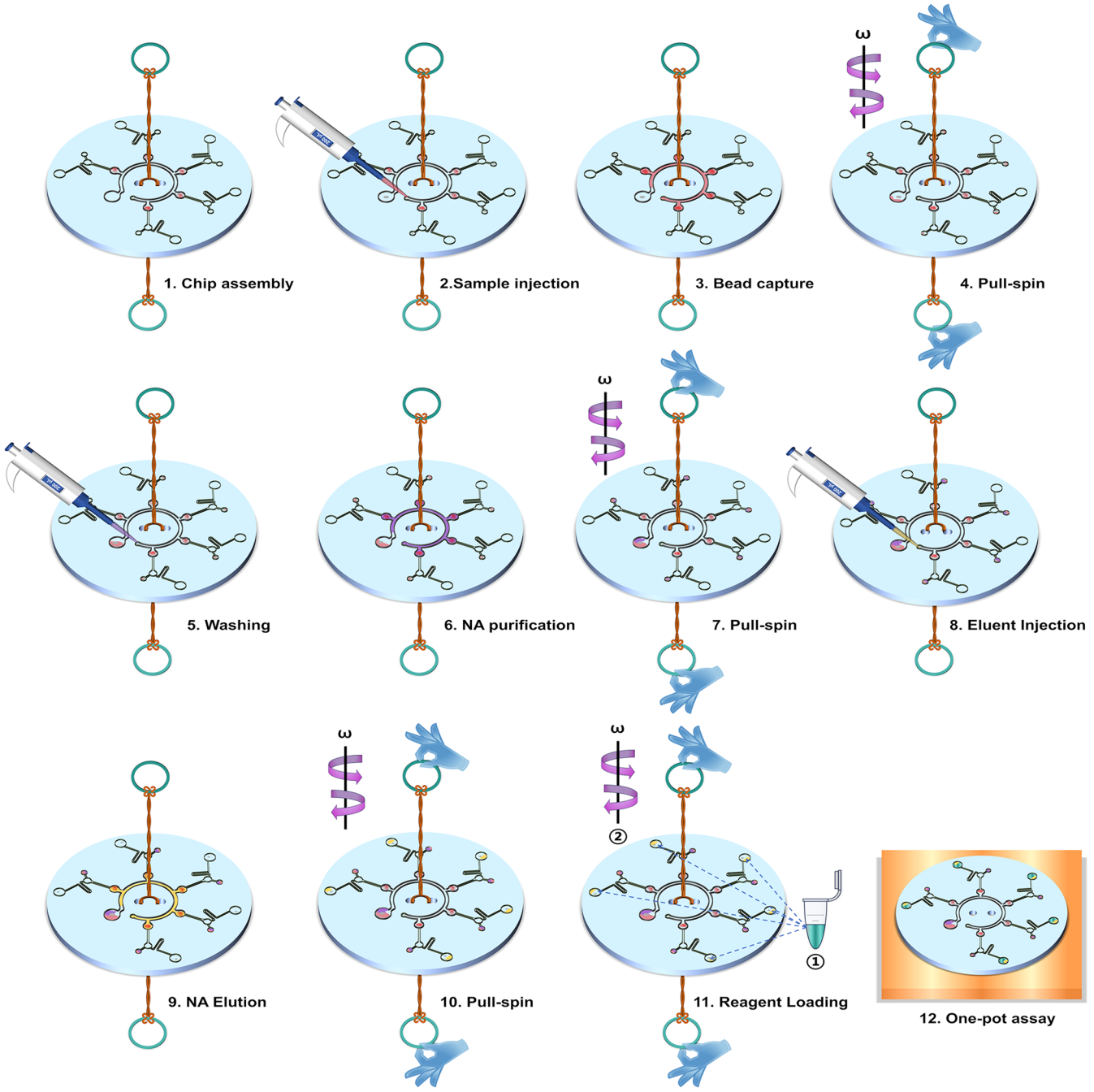


Figure 4. Simplified operating workflow of the HICAS-Chip. The integrated microfluidic device enables sequential on-chip processing, including nucleic acid capture, washing, elution, and one-pot RT-RPA/CRISPR-Cas12a assay. After a 1 h isothermal reaction on a heating block, fluorescence signals are visually observed under UV illumination for rapid identification of HFMD viral subtypes.

end-point fluorescence for any of the four viral subtypes, whereas reducing the RT concentration resulted in a statistically significant enhancement of the signal ($p < 0.05$). This trend is consistent with the findings of Malcı K et al.[43] The results suggest that the overall volume of the one-pot assay system can be decreased without compromising performance, thereby reducing the consumption of costly RPA reagents and offering a practical avenue for lowering expenses.

A comparison of representative one-pot RPA/CRISPR analytical strategies is summarized in Table S5. Unlike approaches relying on physical separation, staged reagent addition, or crRNA modification, the heparin sodium-mediated strategy achieves temporal control through a simple, reversible chemical interaction while preserving a true one-pot format. Table S5 further illustrates that heparin sodium combines moderate sensitivity with minimal cost and operational simplicity, striking a practical balance between performance and usability. While some two-step platforms (e.g., SHERLOCK/DETECTR) achieve slightly higher sensitivity (~1−2 aM), they incur increased reagent cost and procedural complexity. Physical separation or crRNA-modification strategies similarly impose additional design constraints or handling requirements. Herein, the heparin sodium-based method allows universal reagent mixing, and rapid field deployment, making it well-suited for point-of-care applications.

https://doi.org/10.1021/acs.analchem.6c00663
Anal. Chem. XXXX, XXX, XXX−XXX

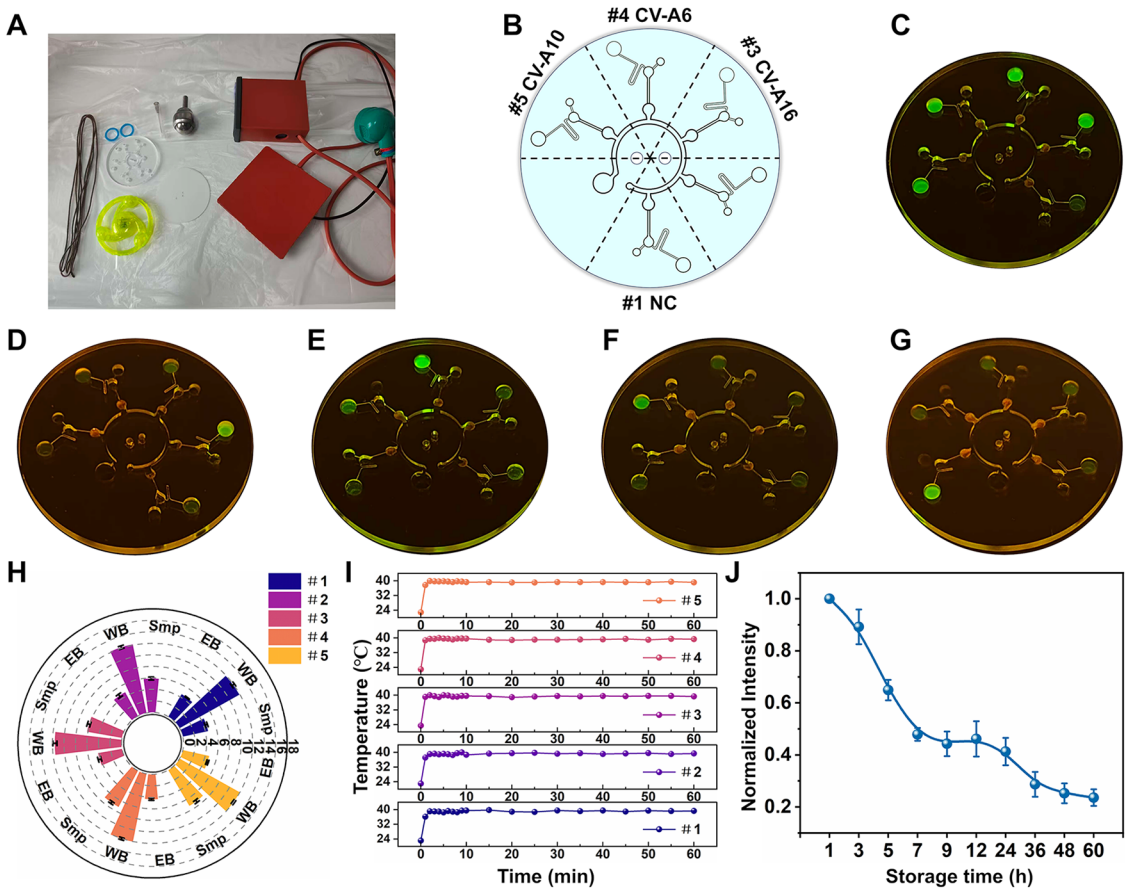


Figure 5. Fluidic characterization and performance validation of the HICAS-Chip. (A) System composition and size comparison with a flywheel toy. (B) Schematic layout of the HICAS-Chip containing five units for target detection and quality control. (C) Simultaneous detection of four nucleic acid targets, confirming reliability under multiplex conditions. (D-G) Specificity tests for (D) EV-A71, (E) CV-A16, (F) CV-A6, and (G) CV-A10; fluorescence signals appeared only in corresponding units, indicating high specificity. (H) Volumes of sample, washing, and elution solutions across different chambers, demonstrating consistent distribution and reproducibility. (I) Temperature profile of the elution chamber, showing rapid heating and stable temperature maintenance for the one-pot reaction. (J) Performance of preloaded one-pot reagents stored at −20 °C, showing retained activity and simplified operation. Data are expressed as mean ± SD (n = 3).

Workflow and Performance of the Integrated HICAS-Chip Device

As illustrated in Figure 3A, the development of the HICAS-Chip involved iterative optimization of the microfluidic device and the integrated detection workflow to ensure stable fluid manipulation and reliable performance. The optimized one-pot RT-RPA/CRISPR reaction was subsequently integrated into the microfluidic device for wastewater analysis. A photograph of the fabricated microfluidic chip is shown in Figure 3B. The structural design of the device is illustrated schematically in Figure 3C, where the HICAS-Chip is composed of a PMMA substrate sealed with a PSA film. The PMMA substrate is the core component of the microfluidic device, and the PSA layer provides encapsulation and pneumatic isolation. As shown in Figure 3D, the PMMA layer integrates functional modules, including an annular main channel, magnetic bead chamber, washing and elution chambers, a siphon valve, and a waste reservoir, which provide the structural basis for nucleic acid enrichment, purification, elution, and one-pot RT-RPA/CRISPR assay.

The detailed workflow of the HICAS-Chip is illustrated in Figure 4, and an operation demonstration of the microfluidic chip is provided in Supporting Video S1. The lysed wastewater samples are first introduced into the chip for microfluidic processing. To ensure stable RNA capture and prevent magnetic beads from precipitating or moving between chambers, magnetic beads supported on glass fiber are preloaded into the bead chambers. This immobilization maintains uniform bead distribution and prevents bead loss during centrifugation, ensuring efficient nucleic acid capture. After loading, the microfluidic chip is sealed with a PSA film. To initiate operation, the PSA layer above the washing chamber is punctured to equilibrate internal pressure. Two 1.5 mm diameter cords are then threaded through the central holes of the chip to enable manual rotation. The sample is introduced through the inlet into the annular main channel and is evenly distributed into the magnetic bead chamber.

Within these chambers, a 5 min incubation is conducted for nucleic acids to bind to the magnetic beads. When the cords are pulled to rotate the chip, unbound components move toward the washing chamber, while nucleic-acid-bound beads remain immobilized within the magnetic bead chamber. Subsequently, 80% ethanol is introduced along the same fluidic pathway to remove impurities. After purification, the punctured hole above the washing chamber is resealed. The PSA layer above the elution chamber is then punctured to rebalance internal pressure, and nuclease-free water is introduced for elution. Another rotation releases the nucleic

https://doi.org/10.1021/acs.analchem.6c00663
Anal. Chem. XXXX, XXX, XXX−XXX

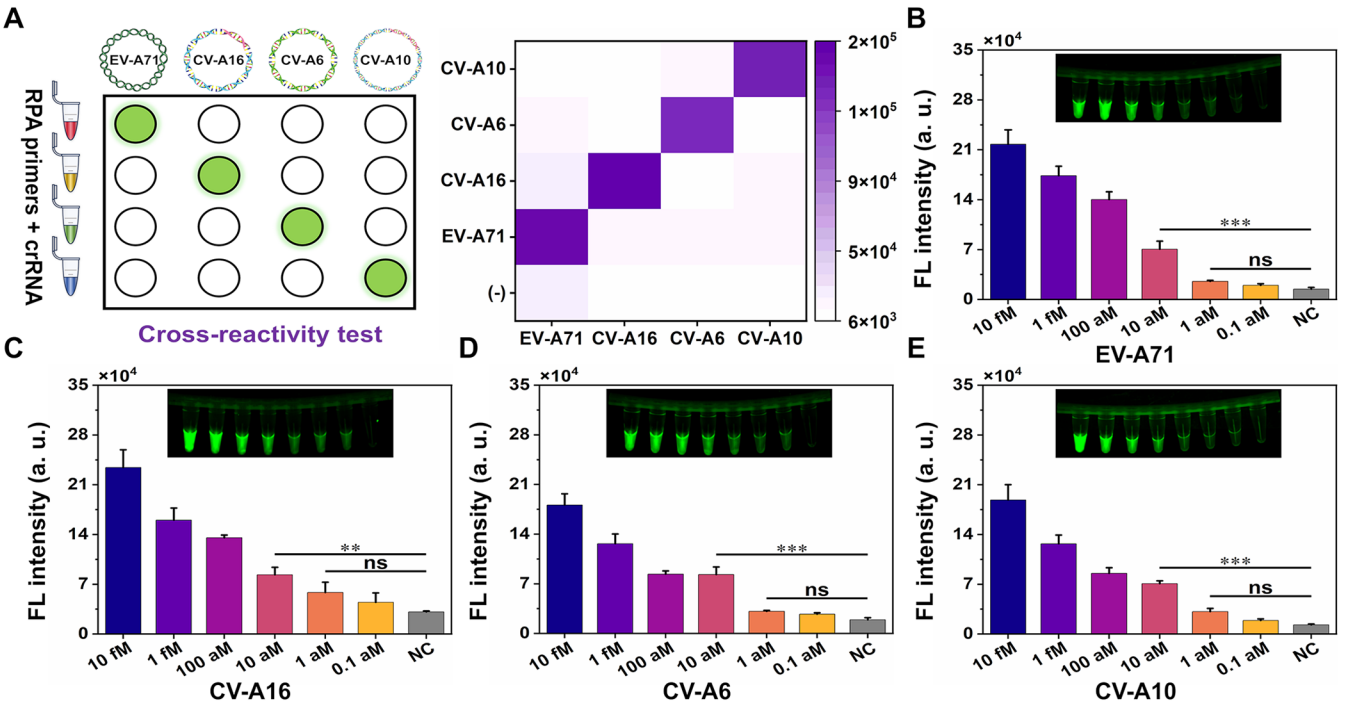


Figure 6. Sensitivity and specificity of the one-pot RT-RPA/CRISPR-Cas12a assay. (A) Fluorescence values obtained from three independent replicates were presented as a heatmap, with each viral RNA target tested in different reaction systems. (B-E) Bar plots showing fluorescence intensities of (B) EV-A71, (C) CV-A16, (D) CV-A6, and (E) CV-A10 at various RNA concentrations, along with corresponding representative fluorescence images. Data are presented as mean ± SD from three independent experiments. Statistical significance is indicated as follows: ns, $p > 0.05$; *, $p < 0.05$; **, $p < 0.01$; ***, $p < 0.001$.

acids from the beads and transfers them into the elution chambers. Following elution, one-pot RT-RPA/CRISPR-Cas12a assay reagents are introduced into the corresponding chambers through the punctured PSA ports without removing the PSA layer. The chip is then placed on a heating block at 39 °C for 1 h, and fluorescence signals are visualized under UV light to determine specific HFMD viral subtypes.

Although reagents were manually added in the current configuration, recent studies have demonstrated that waterproof breathable membranes can be integrated into microfluidic chips to regulate internal pressure and enable sequential reagent delivery.[44,45] Based on this principle, preloading of RT-RPA/CRISPR-Cas12a reagents on the HICAS-Chip is feasible, which could further simplify operation and reduce contamination risks for future field-deployable applications.

As shown in Figure 5A, the size and thickness of the HICAS-Chip are comparable to those of a conventional flywheel toy. During assembly, a roller was employed to achieve precise adhesion between the PSA film and the PMMA substrate, while internal air pressure was balanced using a syringe needle and transparent tape to ensure proper chamber sealing and fluidic stability.[46] As illustrated in Figure 5B, the HICAS-Chip was divided into five independent detection units corresponding to the negative control (#1) and four enterovirus subtypes-EV-A71, CV-A16, CV-A6, and CV-A10 (#2-#5). This physically separated compartment prevents interference posed by multiple target primers, as the case in multiplex PCR.[47] Similarly, a recent LAMP-based chip for influenza virus has used separate chambers per subtype and showed that each channel produces signals only when the target is present without false positives.[48]

To systematically evaluate its detection performance, the multiplexed and synchronous detection capability was first examined (Figure 5C). A mixture containing RNA targets of EV-A71, CV-A16, CV-A6, and CV-A10 at a final concentration of 1 nM was processed through the on-chip washing and elution steps, after which subtype-specific one-pot assay reagents were added into the corresponding chambers. The results demonstrated that all four viral targets were successfully identified, confirming the HICAS-Chip's capability for simultaneous multitarget detection. Furthermore, cross-reactivity validation was performed to assess possible signal interference among units. As shown in Figure 5D−G, distinct fluorescence signals appeared exclusively in chambers containing the corresponding positive targets, while no fluorescence was observed in nontarget or negative control units, indicating excellent interunit independence and the absence of cross-interference within the developed HICAS-Chip platform.

To further evaluate the stability of the HICAS-Chip, fluid dynamics and reproducibility were systematically examined across three key steps: nucleic acid adsorption, washing, and elution. As shown in Figure 5H, following sample injection and centrifugal transfer, excess liquid was efficiently directed into the left washing chamber, with volumes among the five detection units ranging from 4.49 to 7.21 μL. Subsequent washing removed unbound materials into the same chamber, producing a mixed phase of 11.58−12.16 μL, while elution released nucleic acids into the right chamber with stabilized volumes of 4.20−4.67 μL, demonstrating high uniformity and reliable fluidic control. The thermal stability of the chip during isothermal amplification was also assessed by monitoring the chamber temperature with an infrared thermometer throughout a 1 h reaction. As depicted in Figure 5I, the temperature rapidly reached 39 °C within 2 min and remained constant thereafter, confirming rapid heat transfer and stable temperature maintenance suitable for the one-pot reaction. A

https://doi.org/10.1021/acs.analchem.6c00663
Anal. Chem. XXXX, XXX, XXX−XXX

comparative assessment of centrifugal microfluidic driving mechanisms is provided in Table S6; compared with electrically driven platforms, the supercoil-based, human-powered actuation enables bidirectional fluid manipulation with sufficient centrifugal force while markedly reducing system cost and power dependence.

Furthermore, the storage stability of preconfigured detection reagents was investigated using 1 nM RNA targets, with normalized fluorescence used to evaluate performance over time. As shown in Figure 5J, signal intensity decreased by approximately 50% after 24 h of storage, suggesting, in agreement with Liu et al.,[49] that preconfiguration should be performed within 24 h prior to on-site detection to ensure optimal assay reliability.

To evaluate the operation variability of the manually actuated HICAS-Chip, five independent operators performed the HICAS-Chip using the same sample (EV-A71, 100 aM). As shown in Figure S6, all 20 measurements produced fluorescence signals above the threshold, corresponding to a success rate of 100%. The fluorescence intensities obtained from different operators showed consistent signal levels, with an excellent interassay reproducibility (coefficient of variation of 2.74%). These results demonstrate minimal operator-dependent variability of the HICAS-Chip.

Analytical Performance of the HICAS-Chip Assay

Sensitivity and specificity of the one-pot RT-RPA/CRISPR assay were first evaluated in tube-based reactions before integration into the HICAS-Chip. Plasmid-based RNA standards containing the conserved sequences of EV-A71, CV-A16, CV-A6, and CV-A10, were prepared and serially diluted to evaluate the sensitivity of the one-pot RT-RPA/CRISPR-Cas12a assay. As shown in Figure 6B–E, the fluorescence signals were obtained from tube-based reactions, allowing accurate fluorescence quantification and clear visualization of signal differences among target concentrations. Based on visual fluorescence, the optimized one-pot assay achieved a limit of detection (LOD) of 10 aM. As shown in Figure 6A, specificity was evaluated through a heterologous cross-reactivity test. The results demonstrated that each viral RNA target produced a significant fluorescence signal only within its corresponding amplification primer/crRNA reaction system, while no statistically significant response was observed for nonmatched subtypes or negative controls.

Compared with reported one-pot RT-RPA/CRISPR-Cas12a assay strategies without integration, the sensitivity achieved here remains competitive. For instance, Lin et al. reported a glycerol-based physical separation strategy with an LOD of 100 aM.[50] whereas Zeng et al. achieved an LOD of 5 aM using ssDNA-modified crRNA.[24] In addition, the LOD determined by RT-qPCR for standard RNA samples in this study was 1 aM (Figure S3), providing an additional reference for evaluating the sensitivity of the developed method.

Furthermore, the assay was integrated into the HICAS-Chip to evaluate performance in the microfluidic platform. After integration, comparable visual detection sensitivity was maintained. As shown in Figure S7, fluorescence images acquired directly from the chip indicate that fluorescence signals at 10 aM and above can still be reliably distinguished from the negative control by the naked eye, demonstrating that HICAS-Chip did not compromise the sensitivity of the one-pot assay. To further evaluate weak fluorescence signals, quantitative image analysis was performed using ImageJ, where fluorescence was calculated based on the weighted *RGB* formula. As shown in Figure S8, fluorescence intensity gradually decreased with decreasing target concentration from 10 fM to 1 aM. Although the fluorescence signal at 1 aM remained statistically higher than the negative control (defined as mean ± 3SD), its brightness was nearly indistinguishable by the naked eye, whereas concentrations of 10 aM and above could be clearly differentiated visually. These results indicate that the visual LOD of the integrated platform is approximately 10 aM, while image-based fluorescence analysis allows discrimination of signals down to 1 aM.

The sensitivity achieved in this study is comparable to that reported for other centrifugal microfluidic devices and CRISPR-based detection systems. For example, Xu et al. developed a hand-driven centrifugal device for the detection of human papillomavirus (HPV) and achieved LOD of 1 aM and 10 aM for HPV-16 and HPV-18 in clinical samples, respectively.[51] Similarly, Li et al. reported a hand-held spinning-based centrifugal device with an LOD of 3.49 μg mL^{-1} for urinary total protein analysis.[52] However, when fluorescence signals approach the LOD, visual interpretation may become challenging, highlighting the importance of quantitative image analysis for reliable result interpretation.

To assess applicability in real-world samples, the assay was evaluated using wastewater. Viral particles were first concentrated from 250 mL of wastewater to approximately 100 μL during membrane filtration and RNA extraction, corresponding to an approximate 2500-fold enrichment factor. Based on this concentration process, the theoretical detection limit in the original wastewater sample could reach approximately 0.004 aM, indicating the potential capability of the platform to detect low levels of viruses in wastewater.

In wastewater surveillance, detection performance may additionally be influenced by virus recovery rates, RNA extraction yield, and matrix inhibition effects. Nevertheless, the dual recognition mechanism of primer-crRNA targeting effectively eliminates cross-reactivity and enables reliable detection of the four major HFMD-associated viruses. Furthermore, to reduce subjectivity in fluorescence interpretation under field conditions, smartphone-based image acquisition combined with machine learning-assisted analysis represents a promising strategy for automated signal recognition. In our previous work, a CRISPR/Cas12a biosensor integrated with a smartphone-based machine learning model achieved highly accurate fluorescence quantification.[53] Such data-driven approaches could further improve the reliability of weak-signal interpretation in future on-site applications of the HICAS-Chip platform.

Evaluation of HFMD Virus Abundance in Wastewater

To evaluate the recovery rate of the HICAS-Chip, viral RNA standards were spiked into concentrated and lysed wastewater samples, and fluorescence signals from unspiked wastewater were used as the background for correction. Fluorescence images obtained from the spike recovery experiments are shown in Figure S9A–D, illustrating the visual detection performance of the HICAS-Chip for four HFMD viral subtypes (EV-A71, CV-A16, CV-A6, and CV-A10) at different spike concentrations. Based on the quantified fluorescence intensities, recovery rates were subsequently calculated to assess the analytical reliability of the HICAS-Chip. As shown in Figure 7A, the recovery rates of the four viral subtypes ranged

https://doi.org/10.1021/acs.analchem.6c00663
Anal. Chem. XXXX, XXX, XXX−XXX

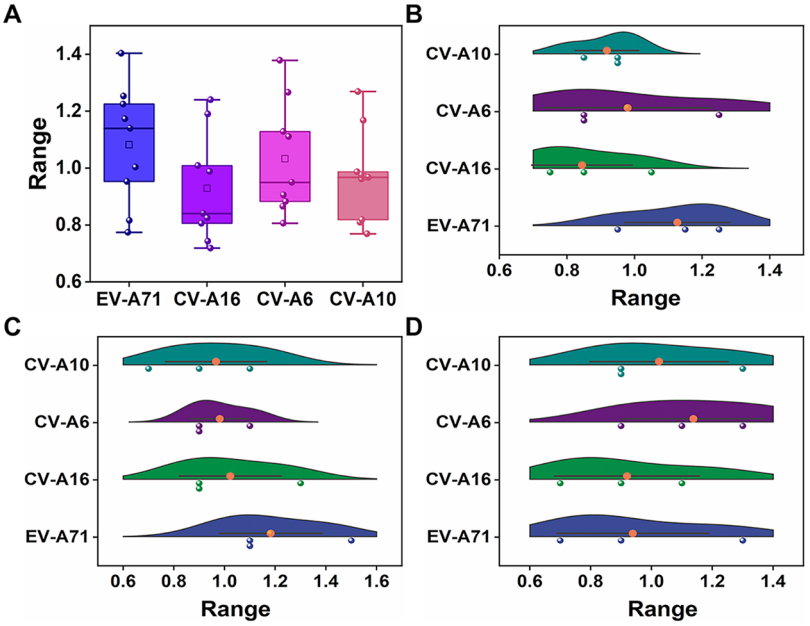


Figure 7. Evaluation of the recovery performance of the HICAS-Chip one-pot assay in complex environmental matrices. (A) Overall recovery rates of four HFMD viral subtypes (EV-A71, CV-A16, CV-A6, and CV-A10) at low (10 aM), medium (100 aM), and high (1 fM) spiking concentrations. (B–D) Recovery rate distributions for each subtype at low (B), medium (C), and high (D) concentrations, respectively. The recoveries ranged from 90% to 110%, with a few outliers slightly above 120% or below 80%. Spike recovery experiments were performed by adding viral RNA standards to RNA extracted from wastewater samples (initial volume: 250 mL); the reported recovery rates reflect only the on-chip processing and detection steps.

from 90% to 110%, with occasional outliers slightly above 120% or below 80%. Specifically, under the low-concentration condition (10 aM), abnormal recoveries were observed for EV-A71 (125.3%), CV-A16 (71.9%), and CV-A6 (126.6%) (Figure 7B). At the medium concentration (100 aM), deviations occurred for EV-A71 (140.3%), CV-A16 (123.0%), and CV-A10 (76.9%) (Figure 7C). At the high concentration (1 fM), several outliers were recorded for EV-A71 (77.4%, 122.5%), CV-A16 (74.3%), CV-A6 (137.9%), and CV-A10 (126.9%) (Figure 7D). Occasional recovery rates exceeding 100% are attributed to stochastic amplification inherent to RPA and potential matrix-induced enhancement effects in complex wastewater samples. These phenomena have been reported for isothermal amplification of nucleic acid.[54−56] Despite these fluctuations, the mean recovery values are acceptable.

The HICAS-Chip was further applied and verified to detect 24 wastewater samples collected from Guiyang City (sampling sites and dates shown in Figure 8A). Fluorescence images obtained from the HICAS-Chip are presented in Figure S10. These images were analyzed using ImageJ to extract mean *RGB* intensity values from each reaction chamber, and the quantified fluorescence signals were visualized as a heat map (Figure 8B).

To evaluate the detection performance of the RT-RPA/CRISPR-Cas12a system, the same 24 wastewater samples were first analyzed using the tube-based one-pot assay, and the results were compared with those obtained by RT-qPCR. Among the 24 samples, EV-A71 showed no negative results in the one-pot assay, whereas one sample each of CV-A16, CV-A6, and CV-A10 yielded fluorescence below the threshold and was classified as negative. Taking RT-qPCR as the reference method, the overall concordance between the tube-based one-pot assay and RT-qPCR was 96.88%. For each viral subtype, scatter plots were generated by plotting RT-qPCR C_t values against the fluorescence intensities obtained from the one-pot assay (Figure 8C–F), showing a strong inverse correlation between the two measurements.

The wastewater samples were further analyzed using the integrated HICAS-Chip. Based on the quantitative analysis of fluorescence images, four samples exhibited fluorescence signals comparable to the negative control and were therefore classified as negative (marked with red circles). Notably, CV-A10 sample #22 showed an *RGB* intensity only slightly higher than that of the negative control and was therefore interpreted as negative. By the naked eye, the fluorescence signal of this sample was difficult to distinguish from the negative control, highlighting the challenge of interpreting extremely weak fluorescence signals based solely on visual inspection, which further supports the use of image-based quantitative analysis to improve interpretation reliability. The three samples that were negative in the tube-based one-pot assay were also classified as negative in the HICAS-Chip analysis, while CV-A10 sample #22 was additionally classified as negative in the on-chip assay. Consequently, the HICAS-Chip achieved an overall detection concordance of 95.83% relative to RT-qPCR, demonstrating high accuracy and stability in complex environmental matrices.

The consistent results with standardized methods have also been reported for other portable platforms. For example, Xiong et al. reported 100% concordance with PCR when analyzing 54 clinical samples using a CRISPR-based system for the simultaneous detection of human coronaviruses.[57] Similarly, Li et al. developed a hand-driven centrifugal device that achieved 100% agreement with standard laboratory methods for determining the minimum inhibitory concentration of antibiotics in 60 clinical samples.[58] Also, Xu et al. reported concordance levels of 98% and 99% with PCR for the detection of HPV-16 and HPV-18, respectively, using a hand-powered centrifugal platform.[51] These comparisons indicate

https://doi.org/10.1021/acs.analchem.6c00663
Anal. Chem. XXXX, XXX, XXX−XXX

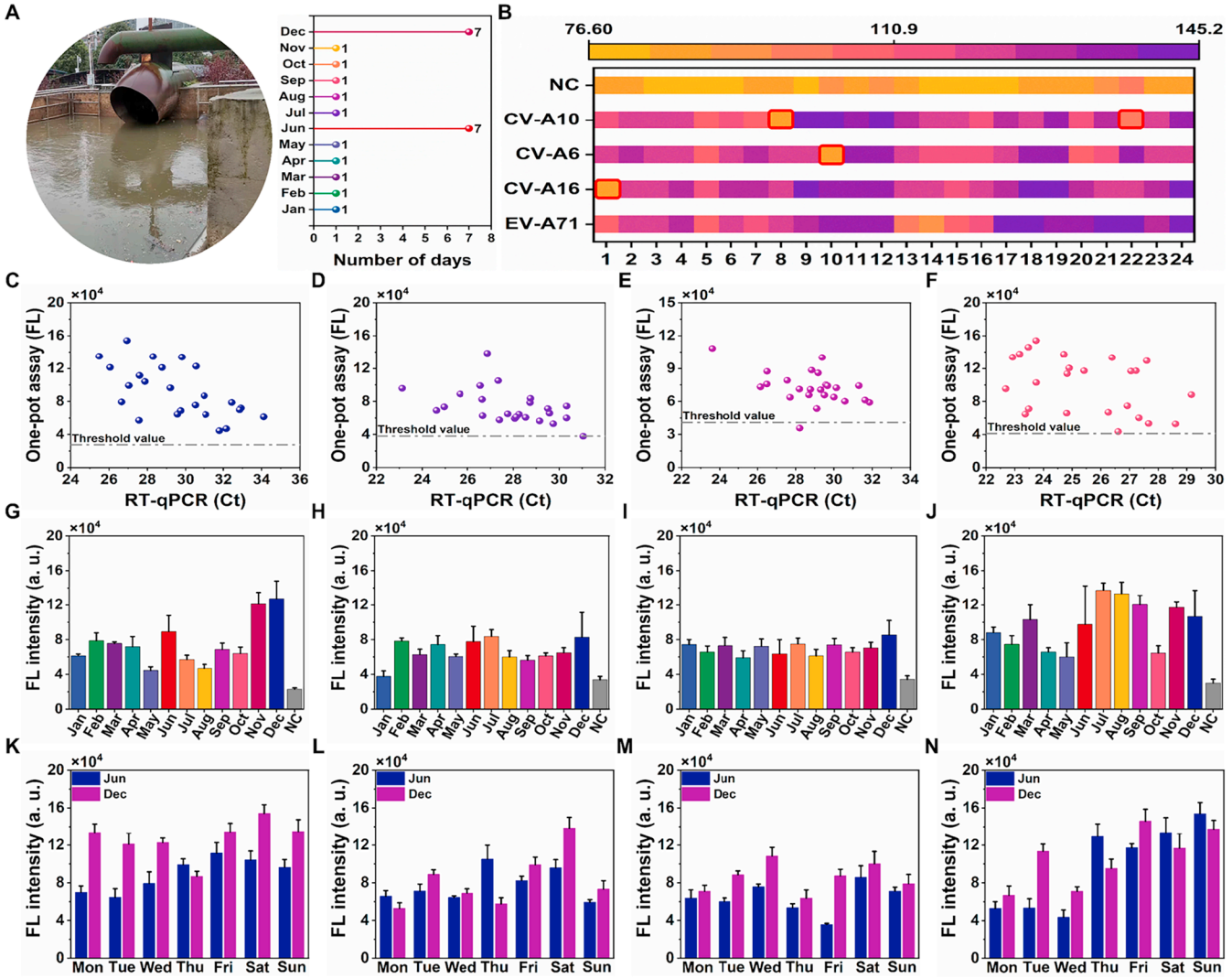


Figure 8. Validation of the HICAS-Chip for detection of HFMD viral subtypes in wastewater with RT-qPCR. (A) Sampling sites and collection dates of 24 wastewater samples from Guiyang City. (B) Heat map of mean *RGB* fluorescence intensity extracted from chip images using ImageJ; samples without detectable signals are marked with red circles. (C–F) Correlation between fluorescence intensity from the one-pot assay and C_t values from RT-qPCR for EV-A71, CV-A16, CV-A6, and CV-A10, showing strong inverse relationships and an overall sensitivity of 96.88%. (G–J) Annual variation in fluorescence signals for the four subtypes, with continuous 7-day sampling in June and December reveals infection peaks in mid- and late-year. (K–N) A detailed 7-day analysis showing pronounced daily fluctuations for EV-A71 and CV-A10, while CV-A16 and CV-A6 exhibited weaker, sporadic signals.

that the analytical performance of the HICAS-Chip, including sensitivity, specificity and concordance with standard laboratory methods, is comparable to previously reported portable platforms. Unlike many existing systems, it also integrates nucleic acid pretreatment and supports multiplex detection for wastewater-based epidemiology.

To further investigate the epidemiological characteristics and temporal dynamics of HFMD within the population, fluorescence signals obtained from the HICAS-Chip assay were analyzed as a time series. Annual monitoring results for the four major viral subtypes-EV-A71, CV-A16, CV-A6, and CV-A10-are presented in Figure 8G–J, with 7-day continuous sampling conducted in June and December. The results revealed that EV-A71 and CV-A10 were the predominant circulating subtypes, exhibiting pronounced increases in June, November, and December, indicating mid- and late-year infection peaks consistent with previous epidemiological reports. For example, a large epidemiological study in Sichuan Province (2011–2017) found incidence peaks in April-July and November-December each year.[59] The dominant serotypes shifted over time and non EV-A71/CV-A16 become more common after 2013.[60] Notably, substantial signal fluctuations were observed in June and December; therefore, a detailed 7-day analysis was performed (Figure 8K–N). As shown, EV-A71 and CV-A10 (Figure 8K,N) displayed significant day-to-day variation across both sampling periods, whereas CV-A16 and CV-A6 (Figure 8L,M) showed generally weaker fluorescence signals, with only sporadic increases on individual days. These variations may reflect factors such as wastewater treatment plant, temporal variations in viral shedding from infected individuals, or differences in sampling times. Overall, continuous wastewater monitoring effectively captured the intensity and distribution of HFMD infections in the community,[61] underscoring the importance of strengthening EV-A71 vaccination coverage and accelerating the development of CV-A10 vaccines.[6] Particularly, the incidence

https://doi.org/10.1021/acs.analchem.6c00663
Anal. Chem. XXXX, XXX, XXX−XXX

of CV-A10 has gradually increased to 25% in China and other East Asian countries.[62]

Overall, these results demonstrate that the HICAS-Chip not only enables sensitive, multiplexed viral detection but also provides a robust platform for rapid community-level surveillance, highlighting its potential for future outbreak monitoring and vaccine assessment.

CONCLUSIONS

The HICAS-Chip developed in this study demonstrates high sensitivity and specificity for the rapid subtyping of major HFMD pathogens. It aligns with the WHO ASSURED criteria for point-of-care testing in resource-limited settings, being sensitive, specific, user-friendly, rapid, and requiring minimal instrumentation. Compared with traditional HFMD detection methods, this platform balances diagnostic performance with operational simplicity. Its reliability and practical utility were further validated through a year-long wastewater-based epidemiology surveillance program.

Despite these advantages, certain limitations remain. The integration of reverse transcription, RPA amplification, and CRISPR signaling within a single reaction presents challenges for precise absolute quantification. User-to-user variability associated with string-powered centrifugal actuation was evaluated and found to be within acceptable limits. Future work could further enhance quantitative performance and system robustness through optimized reaction design, machine learning-assisted analysis, and automated signal processing.

Overall, this portable and low-cost microfluidic platform provides a practical solution for rapid pathogen identification. The HICAS-Chip requires minimal instrumentation and enables on-site wastewater monitoring of HFMD viruses, delivering timely data for early warning, epidemic tracking, and informed public health interventions. Moreover, it exhibits strong potential for extension to other infectious disease control and public health surveillance applications.

ASSOCIATED CONTENT

Supporting Information

The Supporting Information is available free of charge at https://pubs.acs.org/doi/10.1021/acs.analchem.6c00663.

Primer sequences, crRNA and ssDNA reporters, PCR primers, evaluation of one-pot assay strategies, and performance comparison of centrifugal microfluidic driving systems (Tables S1−S6); plasmid linearization, RT-RPA primer screening, PCR standard curves, schematic of the on-chip one-pot workflow, assay performance evaluation, manual operation variability, fluorescence visualization and quantification, spike-and-recovery results, and wastewater sample detection (Figures S1−S10) (PDF)

Video demonstrating the HICAS-Chip operation (Video S1) (MP4)

AUTHOR INFORMATION

Corresponding Authors

Kang Mao − *State Key Laboratory of Environmental Geochemistry, Institute of Geochemistry, Chinese Academy of Sciences, Guiyang 550081, China;* orcid.org/0000-0002-1777-5959; Email: maokang@mail.gyig.ac.cn

Chenglong Tu − *Key Laboratory of Environmental Pollution Monitoring and Disease Control, Ministry of Education, School of Public Health, Guizhou Medical University, Guiyang 550025, China*; Email: tuchenglong@gmc.edu.cn

Authors

Zhen Chen − *Key Laboratory of Environmental Pollution Monitoring and Disease Control, Ministry of Education, School of Public Health, Guizhou Medical University, Guiyang 550025, China; State Key Laboratory of Environmental Geochemistry, Institute of Geochemistry, Chinese Academy of Sciences, Guiyang 550081, China*

Hanqing Meng − *State Key Laboratory of Environmental Geochemistry, Institute of Geochemistry, Chinese Academy of Sciences, Guiyang 550081, China*

Chen Gao − *State Key Laboratory of Environmental Geochemistry, Institute of Geochemistry, Chinese Academy of Sciences, Guiyang 550081, China*

Haoran Lv − *State Key Laboratory of Environmental Geochemistry, Institute of Geochemistry, Chinese Academy of Sciences, Guiyang 550081, China*

Xiqing Li − *Laboratory for Earth Surface Processes, College of Urban and Environmental Sciences, Peking University, Beijing 100871, China;* orcid.org/0000-0002-3162-5068

Qiuda Zheng − *Queensland Alliance for Environmental Health Sciences (QAEHS), The University of Queensland, Woolloongabba 4102 Queensland, Australia;* orcid.org/0000-0002-6456-0926

Zhugen Yang − *Faculty of Engineering and Applied Sciences, Cranfield University, Cranfield MK43 0AL, U.K.;* orcid.org/0000-0003-4183-8160

Ibrahim Ahmed Hamza − *State Key Laboratory of Environmental Geochemistry, Institute of Geochemistry, Chinese Academy of Sciences, Guiyang 550081, China; Department of Water Pollution Research, National Research Centre, Giza 12622, Egypt;* orcid.org/0000-0002-7163-265X

Hua Zhang − *State Key Laboratory of Environmental Geochemistry, Institute of Geochemistry, Chinese Academy of Sciences, Guiyang 550081, China;* orcid.org/0000-0003-4326-7875

Complete contact information is available at: https://pubs.acs.org/10.1021/acs.analchem.6c00663

Author Contributions

Z.C. contributed to conceptualization, methodology, investigation, and writing of the original draft, as well as review and editing. K.M. and C.T. contributed to conceptualization, review and editing, supervision, and funding acquisition. H.M., G.C., L.H., Q. Z., Z.Y., X. L., I.H., and H. Z. participated in manuscript review and editing.

Notes

The authors declare no competing financial interest.

ACKNOWLEDGMENTS

The authors acknowledge the National Natural Science Foundation of China (42377456), the Youth Innovation Promotion Association CAS (2023415), the Hebei Provincial Science and Technology Projects (24291703Z), CAS-ANSO Fellowship (CAS-ANSO-FS-2024-34), and the Guizhou Provincial Science and Technology Projects (Qiankehejichu ZD[2026]147, Qiankexie KJLYRC-[2026]157, Qiankehe Plat-

form Talents-GCC [2023] 046). ZY thanks The Leverhulme Trust Research Leadership Awards (RL-2022−041). We express our gratitude to Professor Hanqing Yu's team at the University of Science and Technology of China for their technical guidance in the one-pot RPA-CRISPR/Cas12 technique.

REFERENCES

(1) Chen, Z.; Mao, K.; Chen, Z.; Feng, R.; Du, W.; Zhang, H.; Tu, C. Isothermal nucleic acid amplification for monitoring hand-foot-and-mouth disease: current status and future implications. *Microchim. Acta.* **2025**, *192* (1), No. 31.

(2) Song, C.; Li, Y.; Zhou, Y.; Liang, L.; Turtle, L.; Wang, F.; Wu, P.; Qiu, Q.; Yang, J.; Wang, K.; Cui, P.; Cheng, Y.; Zhang, T.; Guo, C.; Zeng, M.; Long, L.; Peiris, M.; Zhou, C.; Cowling, B.; Yu, H. Enterovirus genomic load and disease severity among children hospitalised with hand, foot and mouth disease. *EBioMedicine* **2020**, *62*, No. 103078.

(3) Wang, J.; Hu, T.; Sun, D.; Ding, S.; Carr, M.; Xing, W.; Li, S.; Wang, X.; Shi, W. Epidemiological characteristics of hand, foot, and mouth disease in Shandong, China, 2009−2016. *Sci. Rep.* **2017**, *7* (1), No. 8900.

(4) Ooi, M. H.; Wong, S.; Lewthwaite, P.; Cardosa, M.; Solomon, T. Clinical features, diagnosis, and management of enterovirus 71. *Lancet Neurol.* **2010**, *9* (11), 1097−1105.

(5) Mirand, A.; Vié le Sage, F.; Pereira, B.; Cohen, R.; Levy, C.; Archimbaud, C.; Peigue-Lafeuille, H.; Bailly, J.-L.; Henquell, C. Ambulatory Pediatric Surveillance of Hand, Foot and Mouth Disease as Signal of an Outbreak of Coxsackievirus A6 Infections, France, 2014−2015. *Emerging Infect. Dis.* **2016**, *22* (11), No. 1884.

(6) Hong, J.; Liu, F.; Qi, H.; Tu, W.; Ward, M.; Ren, M.; Zhao, Z.; Su, Q.; Huang, J.; Chen, X.; Le, J.; Ren, X.; Hu, Y.; Cowling, B.; Li, Z. J.; Chang, Z. R.; Zhang, Z. J. Changing epidemiology of hand, foot, and mouth disease in China, 2013−2019: a population-based study. *Lancet Regional Health West. Pac.* **2022**, *20*, No. 100370.

(7) Li, X.-W.; Ni, X.; Qian, S.; Wang, Q.; Jiang, R.; Xu, W.; Zhang, Y.; Yu, G.; Chen, Q.; et al. Chinese guidelines for the diagnosis and treatment of hand, foot and mouth disease (2018 edition). *World J. Pediatr.* **2018**, *14* (5), 437−447.

(8) Mao, K.; Zhang, H.; Pan, Y.; Yang, Z. Biosensors for wastewater-based epidemiology for monitoring public health. *Water Res.* **2021**, *191*, No. 116787.

(9) Mao, K.; Zhang, K.; Du, W.; Ali, W.; Feng, X.; Zhang, H. The potential of wastewater-based epidemiology as surveillance and early warning of infectious disease outbreaks. *Curr. Opin Environ. Sci. Health.* **2020**, *17*, 1−7.

(10) Hamza, I. A.; Mao, K.; Gao, C.; Hamza, H.; Zhang, H. Elements of Viral Outbreak Preparedness: Lessons, Strategies, and Future Directions. *Viruses* **2026**, *18* (1), No. 50.

(11) Cao, H.; Mao, K.; Ran, F.; Xu, P.; Zhao, Y.; Zhang, X.; Zhou, H.; Yang, Z.; Zhang, H.; Jiang, G. Paper Device Combining CRISPR/Cas12a and Reverse-Transcription Loop-Mediated Isothermal Amplification for SARS-CoV-2 Detection in Wastewater. *Environ. Sci. Technol.* **2022**, *56* (18), 13245−13253.

(12) Mao, K.; Zhang, H.; Yang, Z. Can a Paper-Based Device Trace COVID-19 Sources with Wastewater-Based Epidemiology? *Environ. Sci. Technol.* **2020**, *54*, 3733−3735.

(13) Shrestha, S.; Malla, B.; Haramoto, E. Monitoring hand foot and mouth disease using long-term wastewater surveillance in Japan: Quantitative PCR assay development and application. *Sci. Total Environ.* **2023**, *901*, No. 165926.

(14) Shrestha, S.; Malla, B.; Sangsanont, J.; Sirikanchana, K.; Ngo, H.; Inson, J.; Enriquez, M.; et al. Detection of enteroviruses related to hand foot and mouth disease in wastewater of Asian communities. *Sci. Total Environ.* **2024**, *912*, No. 169375.

(15) Deng, H.; Gao, Z. Bioanalytical applications of isothermal nucleic acid amplification techniques. *Anal. Chim. Acta* **2015**, *853*, 30−45.

(16) Yang, Z. Low-cost and rapid sensors for wastewater surveillance at low-resource settings. *Nat. Water.* **2023**, *1* (5), 405−407.

(17) Liu, M.; Hou, Y.; Cheng, Y.; Li, Z.; Zeng, J.; Li, L.; Luo, J.; Shen, B. Recent advances in isothermal amplification techniques coupled with clustered regularly interspaced short palindromic repeat/Cas systems. *Interdiscip. Med.* **2025**, *3*, No. e20250052.

(18) Gootenberg, J. S.; Abudayyeh, O.; Lee, J.; Essletzbichler, P.; Dy, A.; Joung, J.; Verdine, V.; et al. Nucleic acid detection with CRISPR-Cas13a/C2c2. *Science* **2017**, *356* (6336), 438−442.

(19) Chen, J. S.; Ma, E.; Harrington, L.; Da Costa, M.; Tian, X.; Palefsky, J.; Doudna, J. CRISPR-Cas12a target binding unleashes indiscriminate single-stranded DNase activity. *Science* **2018**, *360* (6387), 436−439.

(20) Chen, L.; Hu, M.; Zhou, X. Trends in developing one-pot CRISPR diagnostics strategies. *Trends Biotechnol.* **2025**, *43* (1), 98−110.

(21) Ye, X.; Wu, H.; Liu, J.; Xiang, J.; Feng, Y.; Liu, Q. One-pot diagnostic methods based on CRISPR/Cas and Argonaute nucleases: strategies and perspectives. *Trends Biotechnol.* **2024**, *42* (11), 1410−1426.

(22) Feng, W.; Peng, H.; Xu, J.; Liu, Y.; Pabbaraju, K.; Tipples, G.; Joyce, M.; Saffran, H.; Tyrrell, D.; Babiuk, S.; Zhang, H.; Le, X. Integrating Reverse Transcription Recombinase Polymerase Amplification with CRISPR Technology for the One-Tube Assay of RNA. *Anal. Chem.* **2021**, *93* (37), 12808−12816.

(23) Lin, C.; Chen, F.; Huang, D.; Li, W.; He, C.; Tang, Y.; Li, X.; Liu, C.; Han, L.; Yang, Y.; Zhu, Y.; et al. A universal all-in-one RPA-Cas12a strategy with de novo autodesigner and its application in on-site ultrasensitive detection of DNA and RNA viruses. *Biosens. Bioelectron.* **2023**, *239*, No. 115609.

(24) Zeng, Q.; Zhou, M.; Deng, W.; Gao, Q.; Li, Z.; Wu, L.; Liang, D. Sensitive and visual detection of SARS-CoV-2 using RPA-Cas12a one-step assay with ssDNA-modified crRNA. *Anal. Chim. Acta* **2024**, *1309*, No. 342693.

(25) Hu, M.; Qiu, Z.; Bi, Z.; Tian, T.; Jiang, Y.; Zhou, X. Photocontrolled crRNA activation enables robust CRISPR-Cas12a diagnostics. *Proc. Natl. Acad. Sci.* **2022**, *119* (26), No. e2202034119.

(26) Lu, S.; Tong, X.; Han, Y.; Zhang, K.; Zhang, Y.; Chen, Q.; Duan, J.; Lei, X.; Huang, M.; Qiu, Y.; Zhang, D.; et al. Fast and sensitive detection of SARS-CoV-2 RNA using suboptimal protospacer adjacent motifs for Cas12a. *Nat. Biomed. Eng.* **2022**, *6* (3), 286−297.

(27) Huang, D.; He, Y.; Xu, C.; Shen, P.; Li, M.; Fang, M.; Xu, Z.; Fang, X. DNAzyme-Triggered Equilibrium Transfer with Self-Activated CRISPR-Cas12a Biosensor Enables One-Pot Diagnosis of Nucleic Acids. *Anal. Chem.* **2025**, *97* (5), 3026−3035.

(28) Cheng, Z.-H.; Luo, X.; Yu, S.; Min, D.; Zhang, S.; Li, X.; Chen, J.; Liu, D.; Yu, H. Tunable Control of Cas12 Activity Promotes Universal and Fast One-Pot Nucleic Acid Detection. *Nat. Commun.* **2025**, *16* (1), No. 1166.

(29) Thornton, M.; Eder, G.; Amman, F.; Pantielieieva, A.; Vierheilig, J.; Bergthaler, A. Comparative wastewater virome analysis with different enrichment methods. *Water Res.* **2025**, *285*, No. 123985.

(30) Nge, P. N.; Rogers, C.; Woolley, A. Advances in Microfluidic Materials, Functions, Integration, and Applications. *Chem. Rev.* **2013**, *113* (4), 2550−2583.

(31) Zeng, Y.; Khor, J.; van Neel, T.; Tu, W.; Berthier, J.; Thongpang, S.; Berthier, E.; Theberge, A. Miniaturizing chemistry and biology using droplets in open systems. *Nat. Rev. Chem.* **2023**, *7* (6), 439−455.

(32) Phaneuf, C. R.; Mangadu, B.; Tran, H.; Light, Y.; Sinha, A.; Charbonier, F.; Eckles, T.; Singh, A.; Koh, C. Integrated LAMP and immunoassay platform for diarrheal disease detection. *Biosens. Bioelectron.* **2018**, *120*, 93−101.

(33) Linshiz, G.; Jensen, E.; Stawski, N.; Bi, C.; Elsbree, N.; Jiao, H.; Kim, J.; Mathies, R.; Keasling, J.; Hillson, N. End-to-end automated microfluidic platform for synthetic biology: from design to functional analysis. *J. Biol. Eng.* **2016**, *10*, No. 3.

https://doi.org/10.1021/acs.analchem.6c00663
Anal. Chem. XXXX, XXX, XXX−XXX

(34) Natsuhara, D.; Saito, R.; Aonuma, H.; Sakurai, T.; Okamoto, S.; Nagai, M.; Kanuka, H.; Shibata, T. A method of sequential liquid dispensing for the multiplexed genetic diagnosis of viral infections in a microfluidic device. *Lab Chip.* **2021**, *21* (24), 4779−4790.
(35) Xu, Z.; Chen, D.; Li, T.; Yan, J.; Zhu, J.; He, T.; Hu, R.; Li, Y.; Yang, Y.; Liu, M. Microfluidic space coding for multiplexed nucleic acid detection via CRISPR-Cas12a and recombinase polymerase amplification. *Nat. Commun.* **2022**, *13* (1), No. 6480.
(36) Peng, R.; Lu, Z.; Liu, M.; Hu, F. RT-RPA-assisted CRISPR/Cas12a for rapid and multiplex detection of respiratory infectious viruses based on centrifugal microfluidics. *Sens. Actuators, B* **2024**, *399*, No. 134838.
(37) Yuan, H.; Miao, Z.; Wan, C.; Wang, J.; Liu, J.; Li, Y.; Xiao, Y.; Chen, P.; Liu, B. Recent advances in centrifugal microfluidics for point-of-care testing. *Lab Chip.* **2025**, *25* (5), 1015−1046.
(38) Hess, J. F.; Zehnle, S.; Juelg, P.; Hutzenlaub, T.; Zengerle, R.; Paust, N. Review on pneumatic operations in centrifugal microfluidics. *Lab Chip.* **2019**, *19* (22), 3745−3770.
(39) Park, B. H.; Oh, S.; Jung, J.; Choi, G.; Seo, J.; Kim, D.; Lee, E.; Seo, T. An integrated rotary microfluidic system with DNA extraction, loop-mediated isothermal amplification, and lateral flow strip based detection for point-of-care pathogen diagnostics. *Biosens. Bioelectron.* **2017**, *91*, 334−340.
(40) Oh, S.; Park, B.; Jung, J.; Choi, G.; Lee, D.; Kim, D.; Seo, T. Centrifugal loop-mediated isothermal amplification microdevice for rapid, multiplex and colorimetric foodborne pathogen detection. *Biosens. Bioelectron.* **2016**, *75*, 293−300.
(41) Jung, J. H.; Park, B.; Oh, S.; Choi, G.; Seo, T. Integrated centrifugal reverse transcriptase loop-mediated isothermal amplification microdevice for influenza A virus detection. *Biosens. Bioelectron.* **2015**, *68*, 218−224.
(42) Bhamla, M. S.; Benson, B.; Chai, C.; Katsikis, G.; Johri, A.; Prakash, M. Hand-powered ultralow-cost paper centrifuge. *Nat. Biomed. Eng.* **2017**, *1* (1), No. 0009.
(43) Malcı, K.; Walls, L.; Rios-Solis, L. Rational Design of CRISPR/Cas12a-RPA Based One-Pot COVID-19 Detection with Design of Experiments. *ACS Synth. Biol.* **2022**, *11* (4), 1555−1567.
(44) Yuan, H.; Wan, C.; Liu, X.; Dai, C.; Wu, L.; Xie, H.; Wang, X.; Miao, Z.; Li, S.; Li, Z.; Du, W.; Feng, X.; Li, Y.; Qian, C.; Liu, B.; Chen, P. Self-Powered Gravity Domino Microfluidics for Rapid At-Home Immunoassays with Artificial Intelligence. *ACS Nano* **2026**, *20*, 385−404.
(45) Zhao, S.; Guan, X.; Peng, L.; Liu, K.; Zhang, T.; Hu, F. A power-free microfluidic device for the detection of hepatitis B virus in resource-limited settings. *Anal. Chim. Acta* **2025**, *1363*, No. 344154.
(46) Paoli, R.; Di Giuseppe, D.; Badiola-Mateos, M.; Martinelli, E.; Lopez-Martinez, M.; Samitier, J. Rapid Manufacturing of Multilayered Microfluidic Devices for Organ on a Chip Applications. *Sensors* **2021**, *21* (4), No. 1382.
(47) Yang, Y.; Wang, C.; Shi, H.; Guo, X.; Liu, W.; Li, J.; Li, L.; Zhao, J.; Zhang, G.; Song, H.; Hao, R.; Zhao, R. Multiplexed on-site sample-in-result-out test through microfluidic real-time PCR (MONITOR) for the detection of multiple pathogens causing influenza-like illness. *Microbiol. Spectr.* **2023**, *11* (6), No. e02320−23.
(48) Zhao, X.; Gao, J.; Gu, Y.; Teng, Z.; Zhang, X.; Wu, H.; Chen, X.; Chen, M.; Kong, J. LAMP-Based 4-Channel Microfluidic Chip for POCT Detection of Influenza A H1N1, H3N2, and Influenza B Victoria Viruses. *Biosensors* **2025**, *15* (8), No. 506.
(49) Liu, S.; Yang, Y.; Li, X.; Choi, J.; Guo, J.; Luo, H.; Li, C. Development of a single-tube RPA/CRISPR-cas12a detection platform for monkeypox virus. *Biosens. Bioelectron.* **2025**, *278*, No. 117221.
(50) Lin, M.; Yue, H.; Tian, T.; Xiong, E.; Zhu, D.; Jiang, Y.; Zhou, X. Glycerol Additive Boosts 100-fold Sensitivity Enhancement for One-Pot RPA-CRISPR/Cas12a Assay. *Anal. Chem.* **2022**, *94* (23), 8277−8284.
(51) Xu, T.; Zhang, Y.; Li, S.; Dai, C.; Wei, H.; Chen, D.; Zhao, Y.; Liu, H.; Li, D.; Chen, P.; Liu, B.; Tian, Y. Deep Learning-Enhanced Hand-Driven Microfluidic Chip for Multiplexed Nucleic Acid Detection Based on RPA/CRISPR. *Adv. Sci.* **2025**, *12* (21), No. 2414918.
(52) Li, W.; Zhang, J.; Liao, J.; Zhu, M.; Wang, X.; Zhou, X.; Ma, Z.; Hilal, M.; Chua, S.; Tan, G.; et al. A Novel Hand-Held Spinning Platform with Centrifugal Microfluidics for Rapid, Cost-Effective Urinary Total Protein Detection at the Point of Care. *Anal. Chem.* **2025**, *97* (28), 15049−15059.
(53) Xue, J.; Mao, K.; Tang, Z.; Hu, J.; Zhang, H. Machine-Learning-Assisted CRISPR/Cas12a Biosensors for Monitoring Organophosphorus Pesticide Degradation. *Anal. Chem.* **2025**, *97* (39), 21491−21501.
(54) Huang, X.; Lin, X.; Urmann, K.; Li, L.; Xie, X.; Jiang, S.; Hoffmann, M. Smartphone-Based in-Gel Loop-Mediated Isothermal Amplification (gLAMP) System Enables Rapid Coliphage MS2 Quantification in Environmental Waters. *Environ. Sci. Technol.* **2018**, *52* (11), 6399−6407.
(55) Yu, Z.; Man, Y.; Li, W.; Shi, C.; Xiao, P.; Zhang, Q. Light-controlled one-pot RPA-CRISPR/Cas12a biosensor for MRSA detection based on tailed crRNA. *Sens. Actuators, B* **2026**, *448*, No. 138925.
(56) Nwe, M. K.; Jangpromma, N.; Taemaitree, L. Evaluation of molecular inhibitors of loop-mediated isothermal amplification (LAMP). *Sci. Rep.* **2024**, *14* (1), No. 5916.
(57) Xiong, H.; Ye, X.; Li, Y.; Wang, L.; Zhang, J.; Fang, X.; Kong, J. Rapid Differential Diagnosis of Seven Human Respiratory Coronaviruses Based on Centrifugal Microfluidic Nucleic Acid Assay. *Anal. Chem.* **2020**, *92* (21), 14297−14302.
(58) Li, S.; Wan, C.; Wang, B.; Chen, D.; Zeng, W.; Hong, X.; Li, L.; Pang, Z.; Du, W.; Feng, X.; Chen, P.; Li, Y.; Liu, B. Handyfuge Microfluidic for On-Site Antibiotic Susceptibility Testing. *Anal. Chem.* **2023**, *95* (14), 6145−6155.
(59) Peng, D.; Ma, Y.; Liu, Y.; Lv, Q.; Yin, F. Epidemiological and aetiological characteristics of hand, foot, and mouth disease in Sichuan Province, China, 2011−2017. *Sci. Rep.* **2020**, *10* (1), No. 6117.
(60) Yang, B.; Liu, F.; Liao, Q.; Wu, P.; Chang, Z.; Huang, J.; Long, L.; Luo, L.; Li, Y.; Leung, G.; Cowling, B.; Yu, H. Epidemiology of hand, foot and mouth disease in China, 2008 to 2015 prior to the introduction of EV-A71 vaccine. *Eurosurveillance* **2017**, *22* (50), 16−00824.
(61) Shrestha, S.; Malla, B.; Haramoto, E. Evaluation of the Enterovirus serotype monitoring approach for wastewater surveillance of hand foot and mouth disease using secondary epidemiological surveillance data. *Sci. Total Environ.* **2025**, *969*, No. 178896.
(62) An, H.-H.; Li, M.; Liu, R.; Wu, J.; Meng, S.; Guo, J.; Wang, Z.; Qian, S.; Shen, S. Humoral and cellular immunogenicity and efficacy of a coxsackievirus A10 vaccine in mice. *Emerging Microbes Infect.* **2023**, *12* (1), No. e2147022.

https://doi.org/10.1021/acs.analchem.6c00663
Anal. Chem. XXXX, XXX, XXX−XXX